A COMPARATIVE STUDY OF TWO LAND SURFACE SCHEMES IN WRF MODEL OVER EASTERN CHINA

CHEN Liang (陈　亮)[1, 2], MA Zhu-guo (马柱国)[1], FAN Xin-gang (范新岗)[2]

(1. Key Laboratory of Regional Climate-Environment Research for Temperate East Asia, Institute of Atmospheric Physics, Chinese Academy of Sciences, Beijing 100029 China; 2. Department of Geography and Geology, Western Kentucky University, Bowling Green, KY 42101 USA)

Abstract: Two land surface models, Community Land Model (CLM3.5) and NOAH model, have been coupled to the Weather Research and Forecasting (WRF) model and been used to simulate the precipitation, temperature, and circulation fields, respectively, over eastern China in a typical flood year (1998). The purpose of this study is to reveal the effects of land surface changes on regional climate modeling. Comparisons of simulated results and observation data indicate that changes in land surface processes have significant impact on spatial and temporal distribution of precipitation and temperature patterns in eastern China. Coupling of the CLM3.5 to the WRF model (experiment WRF-C) substantially improves the simulation results over eastern China relative to an older version of WRF coupled to the NOAH-LSM (experiment WRF-N). It is found that the simulation of the spatial pattern of summer precipitation in WRF-C is better than in WRF-N. WRF-C also significantly reduces the summer positive bias of surface air temperature, and its simulated surface air temperature matches more closely to observations than WRF-N does, which is associated with lower sensible heat fluxes and higher latent heat fluxes in WRF-C.

Key words: regional climate model; WRF; land surface model

CLC number: P435   **Document code:** A

1 INTRODUCTION

As an important tool of predicting climate change, global climate models (GCMs) have been widely used in large-scale climate prediction. To date, GCMs do not have sufficient spatial resolution to represent regional-scale climate and land surface processes due to limited computational resources. It is even more difficult to describe the meso- and micro-scale (<100 km) interactive process of land surface and climate change, such as vegetation, hydrology, topography, etc., in GCMs for the same reason. According to mechanism studies of regional climate change, GCMs have their great limitations of low spatial resolution[1] and, consequently, its capability of simulating and forecasting regional climate change is very limited. In order to overcome the shortcomings of existing GCMs, regional climate models with high spatial resolution, such as the Regional Integrated Environmental Model System (RIEMS)[2-6]) and the Regional Climate Model (RegCM3)[7-13], have been developed and widely used in studying the regional climate change over China.

Numerous modeling studies have demonstrated that high resolution regional climate models are capable of simulating comprehensive land surface processes and regional climate change interactions[14-16]. In addition to the increase of spatial resolutions for capturing land surface effects, development and improvement of land surface model (LSM) itself has become an important way of enhancing the capability of the regional climate models. Land surface processes affect climate change through the exchange of mass and energy between land surface and the atmosphere. Parameterizing the land surface processes crucially influences numerical weather forecasting and global and regional climate simulations. Coupling more comprehensive treatments of physical processes of land into LSMs has led to reductions of regional climate model uncertainties[17-19]. At present, various regional climate models are developed on the basis of dynamic framework of mesoscale weather forecast models, in which LSMs are coupled.

Along with the fast development of the

next-generation mesoscale numerical weather prediction system, the Weather Research and Forecasting (WRF) model, more and more regional climate simulations have been conducted using the WRF model[15, 20-24].

How to represent land processes is one of the largest uncertainties in climate simulations, as there are few observations to calibrate or constrain them. As we know, different land surface schemes use quite different parameterizations to describe the complex hydrological, biogeophysical and biogeochemical processes. Even when forced by the same atmospheric forcing and provided with the same parameter settings, different land surface schemes can still give significantly different surface fluxes. Therefore, it is very important to study the effect of different land surface schemes on climate simulations. So far, two widely used LSMs have been coupled with the WRF model. One is the Community Land Model (CLM3.5)[25], with reasonable considerations of biophysical and biochemical processes, was developed on the basis of the BATS[26], NCAR/LSM[27], and IAP94[28]. The other is the NOAH LSM. The two land surface models are described in the sections 2.2 and 2.3.

The purpose of this paper is to explore the land surface effects on regional climate change by utilizing the WRF model that is coupled with CLM3.5 and NOAH LSMs and through a comparison study of warm season climate over east China. The newly coupled WRF/CLM3.5 modeling system is denoted as WRF-C and the previously existing coupled WRF/NOAH modeling system is denoted as WRF-N in this paper. Simulations of a typical summer (June, July, August) of 1998 over east China by WRF-C and WRF-N are conducted to validate the newly developed WRF-C modeling system, and then to evaluate the effects of different land surface schemes on regional climate simulations by comparing simulated results to observational data, thereby to investigate the role of the land surface changes in regional climate.

2 THE MODEL AND EXPERIMENTAL DESIGN

2.1 *WRF model*

The WRF model is a joint development effort between the National Center for Atmospheric Research (NCAR), the Forecast Systems Laboratory and the National Centers for Environmental Prediction of the National Oceanic and Atmospheric Administration (FSL, NCEP/NOAA), and the Center for Analysis and Prediction of Storms (CAPS) at the University of Oklahoma, with collaboration from scientists at a number of other universities. The model is intended for use by operational numerical weather prediction and university research communities, providing a common framework for idealized dynamical studies, full-physics numerical weather prediction, air-quality simulation, and regional climate simulation. The WRF is a completely redesigned code, targeted for the 1 to 10 km grid-scale. It will eventually supersede large, well-established but aging regional models now maintained by the participating institutions.

2.2 *NOAH LSM description*

The community NOAH LSM was developed beginning in 1993 through a collaboration of investigators from public and private institutions, spearheaded by National Centers for Environmental Prediction (NCEP). NOAH is a stand-alone, 1-D column model which can be applied in either coupled or uncoupled mode. The NOAH LSM is used to predict soil moisture and temperature at 4 layers with thicknesses, from top to bottom, of 10, 30, 60, and 100 cm, respectively, as well as canopy moisture and water-equivalent snow depth. The NOAH LSM has one canopy layer, and its total depth of soil layers is 2 m. The upper 1 m of soil serves as the root zone depth, and the lower 1 m of soil serves as a reservoir with gravity drainage[29].

2.3 *CLM3.5 model description*

The CLM3.5 was the NCAR version of CoLM (Common Land Model) that was originally developed by Dai[28] on the basis of the BATS, NCAR/LSM, and IAP94, which has been adopted by the NCAR/CCSM (Community Climate System Model)[25]. CLM3.5 represents a "third-generation" land surface model, which includes a physical representation of the coupling between the water, energy, and carbon cycles. The CLM3.5 calculates the land surface variables at each model grid point with ten unevenly spaced soil layers, one vegetation layer with a canopy photosynthesis-conductance model, and up to five snow layers depending upon the total snow depth. Soil temperature and soil moisture are solved with explicit treatment of liquid water and ice. Runoff is calculated from surface and base flow for saturated and unsaturated regions. CLM3.5 was coupled into WRF version 3 by Jin et al.[30-32].

A brief comparison of the features and differences between land surface schemes NOAH and CLM3.5 is given in Table 1. CLM3.5 is a more complex model than NOAH because of its finer vertical soil and snow layer resolution, tiling structure, subsurface lateral runoff and direct calculation of carbon.

Table 1. Comparison of the NOAH and CLM3.5 land surface schemes in WRF.

	Soil	Snow	Vegetation	Lake	River Routing
NOAH	4 layers of soil moisture, soil temperature, and frozen soil	1 layer of snow (the top soil layer)	Only one vegetation type in one grid cell, no dynamic vegetation or carbon budget	N/A	N/A
CLM3.5	10 layers of soil moisture, soil temperature, and frozen soil	5 layers of snow	Up to 10 vegetation types in one grid cell with dynamic vegetation and carbon budget	10 layers of lake including lake ice and snow	A Digital Elevation Model to calculate water flow directions

2.4 *Experimental design*

In this work, simulation experiments by WRF-C and WRF-N for summer climate of the year 1998 over east China are undertaken to validate the newly coupled model WRF-C. During the summer 1998, extremely heavy rain took place in Yangtze River basin (between 26–32°N). The model domain is therefore centered at 30°N, 115°E, and the Lambert conformal map projection is adopted. Figure 1 shows the model domain and topography. The model configuration is resumed in Table 2. The model grid consists of 91 (west-east) by 97 (north-south) grid lines at approximately 30 km horizontal resolution, and 18 sigma levels in the vertical. Initial conditions and large-scale forcing are obtained from the 6-hourly NCEP-DOE reanalysis (R-2) data. The simulation period is the whole year of 1998, but in this study, we only analyzed the summer time. To validate simulated results, we used the following datasets: the observed daily precipitation and temperature at 730 Chinese meteorological stations, obtained from the Chinese National Meteorological Center, and the Global Precipitation Climatology Project (GPCP) daily precipitation with horizontal resolution of 1° by 1°[33].

3 SIMULATION RESULTS

3.1 *Precipitation*

Summer total precipitation in China is mainly dictated by the Asian Monsoon system. Generally, the precipitation is formed in west-east-oriented bands, which progress or retreat with time and in the south-north direction. Sometimes, the precipitation bands may appear to skip some latitudes. In 1998, the precipitation in most parts of China presented a positive anomaly compared to normal conditions that are usually defined as a long-term average. Figure 2 shows spatial distributions and patterns of observed and model simulated precipitation in June (left), July (middle) and August (right) 1998 over east China. It is

shown that the early-Meiyu period over the Yangtze River basin appeared in June, and the rainstorm region is mainly located in the areas to the south of 30°N with two rainfall centers (Figure 2a). WRF-C generated reasonably well spatial patterns of precipitation over East China. In particular, the locations and spatial coverage of the two rainfall centers in the areas to the south of Yangtze River basin are well captured compared to observations (Figures 2a and 2d). Although WRF-N also generated precipitation around the two rainfall centers, the intensity and scope of precipitation is very much overestimated in the South China area but underestimated in the areas to the south of Yangtze River basin (Figure 2g).

Figures 2b, 2e, and 2h indicate that, in July, WRF-C reproduced the rain band over the Yangtze River basin with right magnitude, while WRF-N failed to generate any precipitation in the area; instead, WRF-N placed a rainfall center over Sichuan Basin near the west border of the domain. For the area of west South China over Yunnan-Guizhou Plateau, both models overestimated the precipitation amount, while WRF-C showed closer results to the observations than WRF-N did.
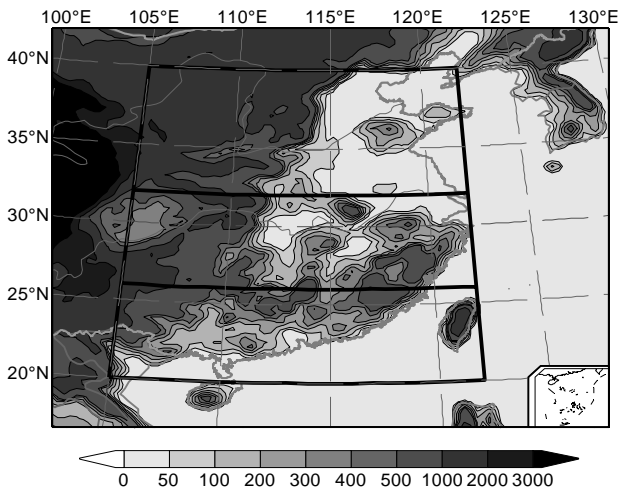
Figure 1. Model topography in meters obtained based on the USGS high-resolution dataset. The three areas confined by thick lines between 105–122°E show three regions that are used for areal averaging and analysis later. South China: 20–26°N; Central China (Yangtze River basin): 26–32°N; North China (Yellow River Basin): 32–40°N.

In August (see Figures 2c, 2f, and 2i), WRF-C well captured the position and scope of the rain band from the northeast to the southwest between the Yangtze River basin and the Yellow River basin, though the simulated precipitation is smaller than

observations in the lower reaches of Yellow River basin. The less intensive rain band along southeast coastal areas in South China was missing from WRF-C simulations. WRF-N was able to generate a rain band but it was largely displaced farther north, except the west-end of the rain band, and the precipitation amount is even smaller than in WRF-C. While WRF-N also missed the rain band in South China and southeast coastal areas, it also produced a false heavy rainfall center in Yunnan-Guizhou Plateau.

Table 2. Model Configuration.

| Model prototype	WRF/ARW (version 3.0)
Simulation period	Jan 1-Dec 31, 1998
Vertical layers (top)	18 layers (50 hPa)
Horizontal resolution	30km
Horizontal grid number	96×90
Integral time-step	180 sec
Cumulus convection	Kain-Fritsch (new Eta) scheme
Mp_physics	WSM5-class
PBL	YSU
Short/Long Radiation	RRTM/Dudhia
Land surface	Noah LSM/CLM3.5
Driving Data	NCEP/DOE Reanalysis 2
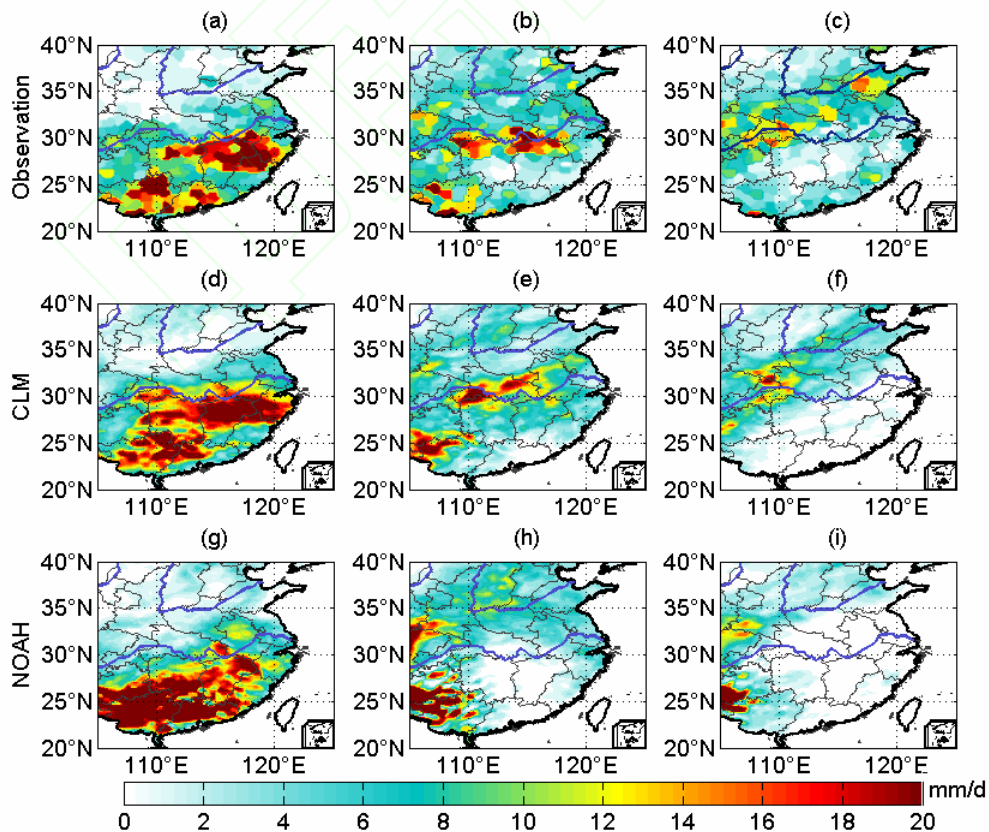
Figure 2. Spatial distributions of observed and modeled monthly-averaged precipitation rates in June (left panels), July (middle panels) and August (right panels) 1998 (Units: mm/day). (a), (b) and (c): Observed; (d), (e) and (f): WRF-C simulated; (g), (h) and (i): WRF-N simulated.

The spatial distributions of monthly precipitation results show better overall simulations in WRF-C than in WRF-N in terms of spatial patterns, position of rain bands and centers, and rainfall intensity.

In order to investigate further the different impacts of the two models on precipitation simulation, the summer average precipitation (SAP, for June, July, and August) is studied in more detail for the three subregions as shown in Figure 1. In the South China region, WRF-N predicted ~40 mm/month (~30%) less SAP than observed, while WRF-C predicted ~97 mm/month (~125%) less SAP than observed. The underestimates with both models were mainly from the missed rain band along southeast coastal areas in August as described above and shown in Figure 2. The superior simulation of WRF-N relative to WRF-C in the South China region relates to the intensive precipitation in June and overestimates in July and August in Yunnan-Guizhou Plateau area. In the Yangtze River region, WRF-N predicted ~119 mm/month (~162%) less SAP than observed, while WRF-C predicted ~18 mm/month (~10%) less SAP than observed. In the Yellow River region, WRF-N predicted ~59 mm/month (~53%) less SAP than observed, while WRF-C predicted ~33 mm/month (~24%) less SAP than observed. Obviously, the simulation results of WRF-C are superior to those of WRF-N for both the Yangtze River region and the Yellow River region, which complies with the better spatial distribution and placement in the WRF-C model results as discussed above.

Catastrophic floods occurred over the Yangtze River basin during the summer of 1998 when the East Asian Summer Monsoon circulation and South China Sea Summer Monsoon were obviously weaker than normal[34, 35]. This is because that, in a weak Asian summer monsoon year, the effect of advection caused by monsoon on regional rainfall is consequently minimal, whereas the effects of land surface processes become dominant and have stronger impacts on local or regional climate. The superior modeling results of WRF-C to WRF-N for the Yangtze River Basin reflect the important impact of different treatment of land surface processes on precipitation.

3.2 *Precipitation description*

Northward migration of the subtropical front and associated rain band is one of the prominent features over East China, which is a major effect from the Asian summer monsoon. It determines the basic spatial and temporal patterns of rainfall in this region. This type of seasonal march of the major monsoon precipitation band appeared in summer 1998 too (as illustrated in Figure 3), which shows the time-latitude cross-section of averaged precipitation rates along the longitudinal band between 105–122°E over eastern

China (see Figure 1 for the location of the longitude band). The GPCP data is used to validate the model precipitation. The observed time-latitude cross-section (Figure 3a) shows that the rain band oscillated between the north and south bounds of 18°N and 40°N from early May to early June. From May 1, although the precipitation amount was small, the rain band quickly retreated southward to 20°N and then migrated northward to about 35–40°N. From May 10, the rain band began to retreat southward and then remained in the South China area until May 17. In early June, there were two rain bands, an intensive band in South China and a weak band in North China. The one in South China migrated northward from 18°N in early June to 40°N in mid-July. The average speed of northward movement was approximately 0.5° latitude per day (~55 km/day). The northward migration reflected the seasonal march of the East Asia summer monsoon. From July 13, the rain band began to retreat quickly southward and maintained near 28°N around July 20th, and it caused the second Meiyu period over the Yangtze-Huaihe Rivers basin.

Figures 3b and 3c show that there exist remarkably different simulation results between WRF-C and WRF-N from May 1 to early June. The simulation by WRF-C matches more closely with the observations than WRF-N does. The rain band of the WRF-N simulations oscillates north-south with time and mostly remains stable around 25°N; they are also stronger than observations. From early June to mid-July, both the WRF-C and WRF-N simulations captured the observed northward migration process of the rain band. The WRF-C was able to capture the southward retreat of the rain band successfully. In comparison, WRF-N failed to simulate the heavy rainfall during the southward retreat but instead, the rain band jumped directly to the area around 28°N with only a smaller amount of rainfall than observations. Figures 3b and 3c also indicate that both WRF-C and WRF-N failed to simulate the precipitation over South China, as discussed above. In general, the northward migration process simulated by WRF-C was improved in comparisons to WRF-N, especially in early and late summer.
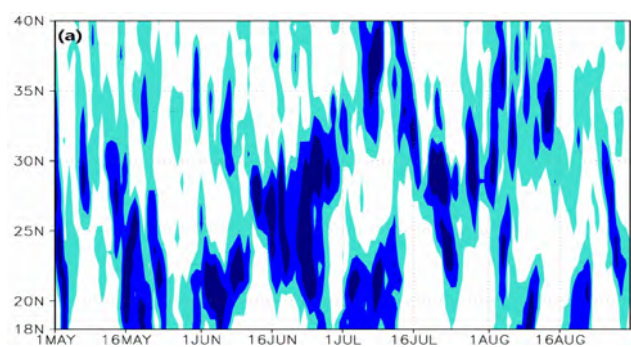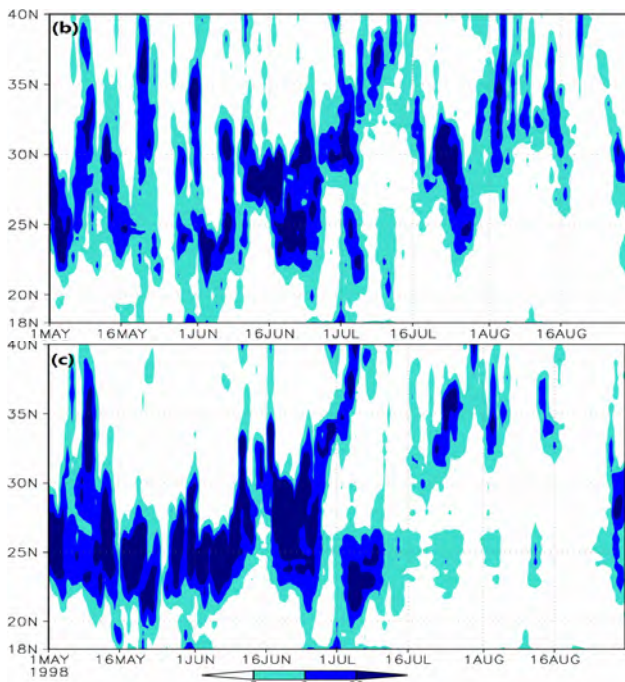
Figure 3. Time-latitude cross-sections of daily precipitation rates (mm day^{-1}) in eastern China averaged between 105ºE and 122ºE of the model domain from May 1 to August 31, 1998, which were derived from (a) observations, (b) WRF-C simulations, (c) WRF-N simulations. The observations were based on GPCP.

For further examination of the ability of the two modeling systems in simulating the regional summer precipitation in east China, Figure 4 shows the comparisons of precipitation in WRF-C and WRF-N with observed precipitation for the three sub-regions shown in Figure 1. Figure 4a shows the simulation results over north China in summer 1998. Although the WRF-N precipitation trend is similar to the observations, its correlation coefficient with GPCP is very low, only 0.08, while in comparison, the correlation coefficient between WRF-C and GPCP is 0.57. Figure 4b shows that WRF-N overestimated precipitation in early summer but underestimated it in late summer for the Yangtze River region; the WRF-C precipitation matches the observations more closely than WRF-N throughout the whole summer. The correlation coefficient is 0.55 between WRF-C and GPCP and 0.37 between WRF-N and GPCP. Figure 4c shows the simulation results over South China in summer 1998. Both WRF-C and WRF-N simulations were able to capture the major precipitating events. WRF-N overestimated the precipitation between early May and early July, while WRF-C simulation is closer to the observations. From mid-June to early July, the two simulations are all very close to each other and to the observations. From the early July, both simulations underestimated the precipitation. The correlation coefficient between WRF-C precipitation and GPCP data is 0.55, while it is only 0.39 between WRF-N and GPCP. The conclusions drawn from the

precipitation simulations reflect the fact that the influence of Asian monsoon decreases from south to north. Therefore, the improvement of land surface schemes demonstrated most significant effect on precipitation simulations in North China, followed by Yangtze River region and South China, respectively. The improvement on precipitation simulations is determined by the relative degree of influence from the Asian monsoon and the improved land surface schemes.
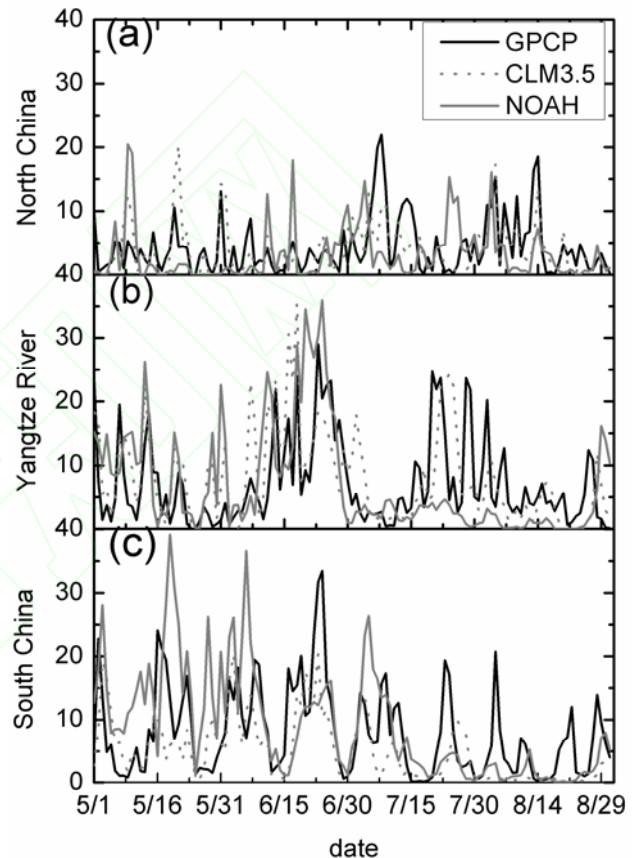

Figure 4. Observed and modeled precipitation rates for the three regions of East China in summer of 1998 (Unit: mm/day). (a): North China; (b): Yangtze River; (c): South China.

3.3 *Surface air temperature*

Figure 5 is the spatial patterns of observed and modeled surface air temperature (SAT, in °C) at 2-m height in June (left), July (middle) and August (right) 1998. The observed 2-m SAT data from the 730 stations are interpolated onto the model grids as shown in Figures 5a to 5c. The major spatial patterns show consistency with topography, i.e., it is warm in plains and low-terrain regions and cold in high-terrain regions. Figure 5 indicates that the spatial patterns of monthly averaged SAT in summer are well simulated by both WRF-C and WRF-N, whereas the simulation of WRF-C matches more closely the observations than WRF-N does. In June, both the WRF-C and WRF-N results are very close to the observation except for a small cold bias in South China and a

small warm bias in North China. In July and August, compared to the observations, both the WRF-C and WRF-N simulations have warm biases over most of the region (to the north of 25°N) except for cold biases in South China (to the south of 25°N), while WRF-C has significantly smaller warm biases than WRF-N over most of the region, especially over areas of Yangtze River basin and North China. WRF-C also

has smaller cold biases than WRF-N over the South China area. Overall, the SAT simulation by WRF-C is superior to that of WRF-N in the summer 1998 over East China. The results above suggest that the near-surface air temperature simulation has been greatly improved by coupling more complex land surface processes that are represented by the CLM3.5 in the WRF model.
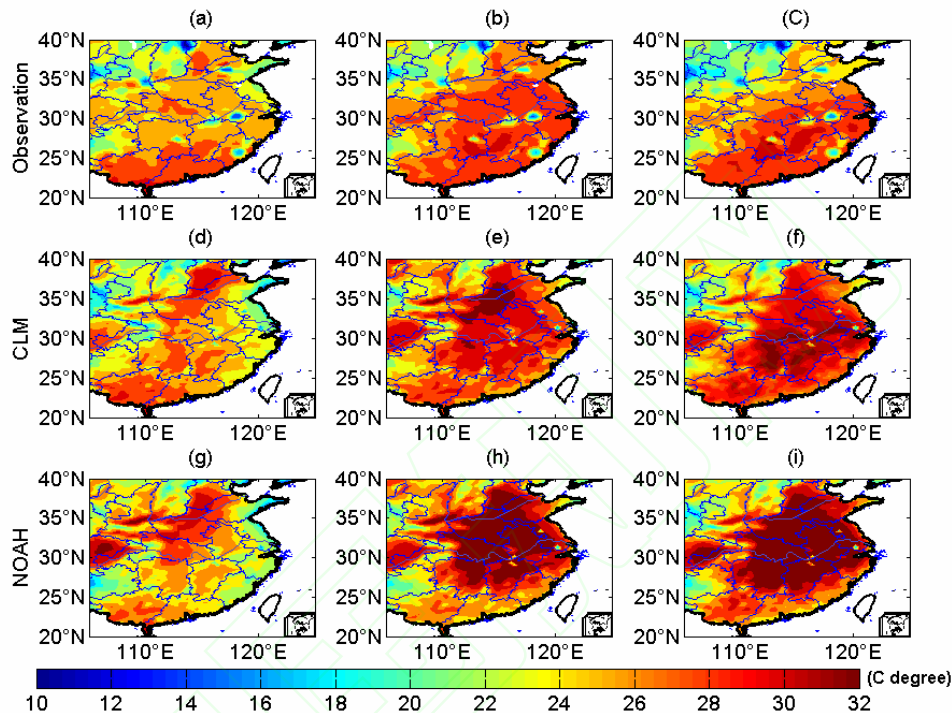

Figure 5. Spatial patterns of observed and modeled 2-m air temperature in June (left panels), July (middle panels) and August (right panels) 1998 (Unit: °C). (a), (b) and (c): observational data in China; (d), (e) and (f): WRF-C simulation; (g), (h) and (i): WRF-N simulation.

3.4 *Interpretation of the results*

Land surface processes are primarily driven by precipitation and solar radiation; they also exert feedback to the atmosphere through surface energy, water and momentum fluxes[36]. Here we attempt to study some of the possible rationales regarding the improvement in precipitation and surface air temperature simulations produced by WRF-C. Emphasis is given on the analysis of circulation patterns, and energy and moisture transport. When the circulation pattern changes, it will transport energy and moisture to different places, consequently affecting the spatial distribution of air temperature and precipitation.

From the analysis in sections 3.1 and 3.2, we found that during the summer of 1998, the simulation of the spatial pattern of precipitation in WRF-C is generally better than in WRF-N. Figure 6 shows the monthly average 850 hPa wind vectors for WRF-C simulations and WRF-N simulations, along with NCEP reanalysis for the three summer months of 1998. In June, Yangtze River basin and South China

are controlled by a southwest air stream. The subtropical high is on the east side of the domain and over the western Pacific Ocean[37]. Both WRF-C and WRF-N simulated the large scale 850 hPa wind patterns reasonably well when compared to NCEP reanalysis, but the WRF-C and WRF-N runs show more details. Yunnan-Guizhou Plateau and Sichuan basin are in the low-pressure regions. This flow pattern helped transporting warm moist air from the southern oceans and seas to East China. Comparing the wind patterns of WRF-C and WRF-N simulations in Figure 6, it is found that WRF-N simulated a much stronger southwest low-level jet over the Yunnan-Guizhou Plateau in the southwest of China than WRF-C did. Furthermore, the cyclonic air flow surrounding the Sichuan Basin in the WRF-N simulations is also stronger than in the WRF-C simulations. The cyclonic flow pattern gradually weakened from June to August. This well explains why WRF-N has produced excessive precipitation in June in the Sichuan Basin and Yunnan-Guizhou Plateau.
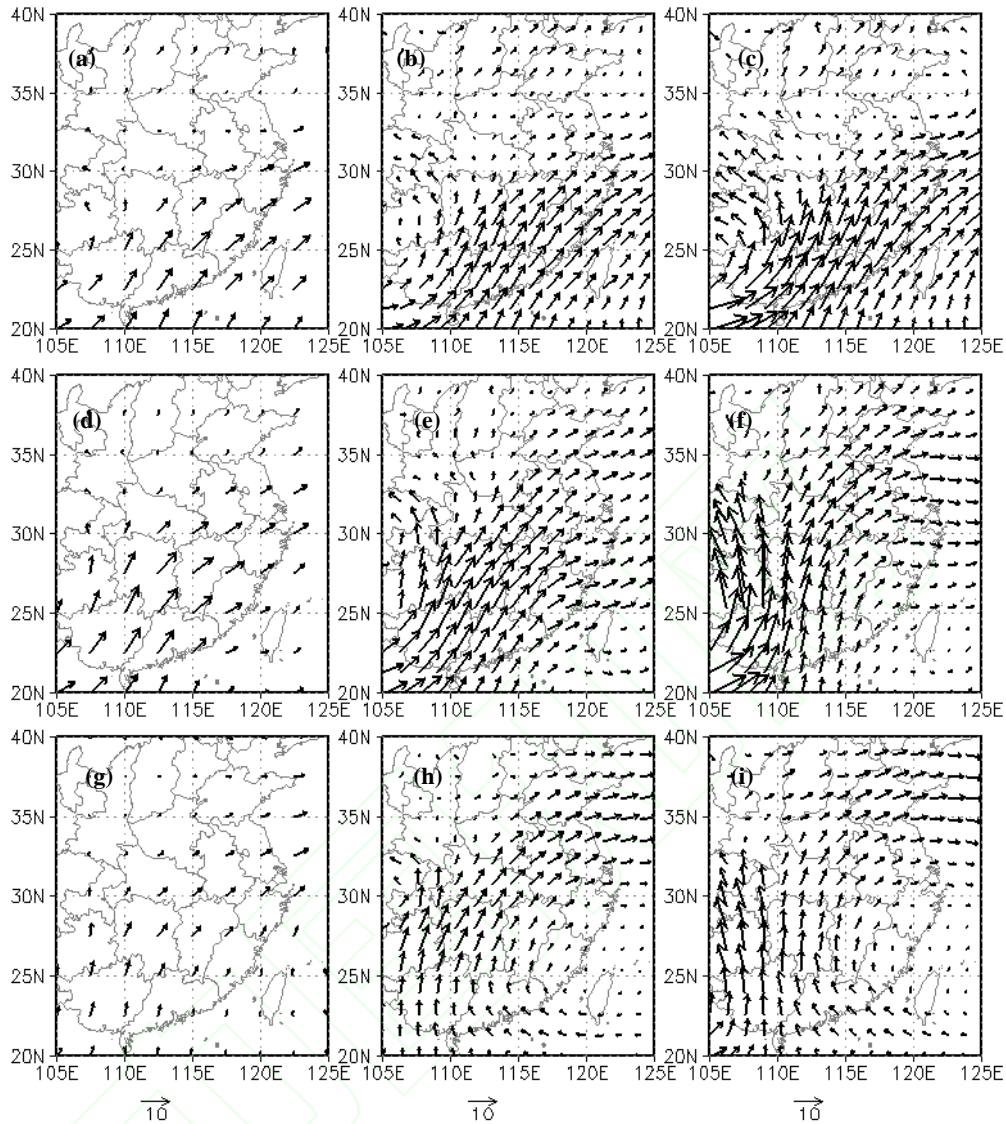
Figure 6. Monthly average 850 hPa wind vectors for NCEP reanalysis (left panels), WRF-C simulations (middle panels), and WRF-N simulations (right panels) in the three summer months of 1998. (a), (b) and (c): June; (d), (e) and (f): July; (g), (h) and (i): August.

To gain further insight to the model simulation of precipitation, the column integrated kinetic energy (KE) and the column integrated moisture flux convergence (MFC) are calculated. MFC has been used in the practice of predicting convective initiation[38]. The KE is computed using a stepwise integration downwards through the column, divided by the pressure depth of the (model) atmosphere[39]. For each *i, j* point:

$$KE_{ij} = \frac{1}{g(P_S - P_{Top})} \int_{P_{Top}}^{P_S} \frac{1}{2}(u^2 + v^2 + w^2)dp \quad , (1)$$

where P_S is the surface pressure, P_{Top} the pressure at the top level of the model, and *u*, *v*, and *w* correspond to the zonal, meridional and vertical wind speed, respectively.

The MFC is calculated by

$$MFC_{ij} = -\frac{1}{g} \int_{P_{300}}^{P_S} \nabla \cdot (q\vec{v})dp . \quad (2)$$

Here $P_{300} = 300$ hPa, P_S is the surface pressure, *g* the acceleration due to gravity, *q* the specific humidity, and $\vec{v}$ the horizontal velocity vector. Positive values of MFC mean convergence of moisture.

Figure 7 shows the differences of KE among simulations of WRF-C and WRF-N and NCEP reanalysis. It is shown that the distribution of KE is quite different between WRF-C and WRF-N (Figures 7g to 7i). The differences between WRF-C and NCEP2 or between WRF-N and NCEP2 are consistent with the heavy rain locations (Figures 2 and 7), which implies that the downscaling simulations in high resolution WRF models not only added values in these areas, but also contributed, in the meantime, to

the precipitation. By comparing Figure 7 to Figure 2, it is found that the large positive KE difference areas correspond to the heavy rainfall areas. In June, the rainstorm region is mainly located in the areas to the south of 30°N with two rainfall centers. In the rain areas, the KE of WRF-C and WRF-N also have large biases (Figures 7a and 7d). In July, WRF-C has a large KE difference in the Yangtze River basin (Figure 7b), while WRF-N has a small one (Figure 8e),

which may explain why WRF-C can capture the precipitation well in the Yangtze River basin while WRF-N cannot. In August, like in July, WRF-N also had a very large KE difference in Southwest China (Figure 8f) and failed to capture the northern rain belt, while WRF-C captured the rain belt well. The KE differences between WRF-C and WRF-N (Figures 7g to 7i) can reflect the differences in the simulated precipitation by the two models.
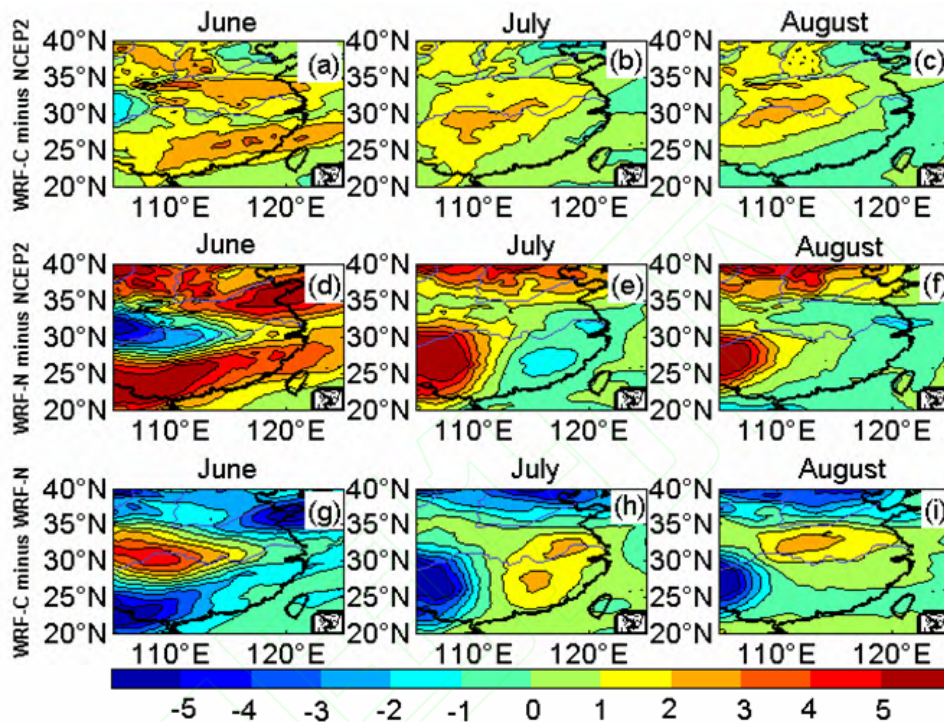

Figure 7. The difference of the Kinetic Energy (KE) of (a), (b) and (c) for WRF-C minus NCEP2, (d), (e) and (f) for WRF-N minus NCEP2, (g), (h) and (i) for WRF-C minus WRF-N, in June (left panels), July (middle panels) and August (right panels) 1998.

In addition to the KE analysis, Figure 8 shows the differences of MFC among simulations of WRF-C and WRF-N and NCEP reanalysis. Areas of negative values on the MFC difference maps are showing reduced water vapor convergence in those areas. Figures 8g to 8i show large areas of negative values, which means that WRF-C has smaller moisture convergence than WRF-N. This is consistent with the fact that the WRF-C produced smaller amount of precipitation than WRF-N. Both WRF-C and WRF-N show added high resolution features of water vapor convergences compared to NCEP reanalysis. However, since the reanalysis is even coarser in resolution, the difference fields of MFC do not necessarily reflect the

precipitation differences between model simulations and observations.

Regarding to the temperature differences between the two models, WRF-C has significantly smaller positive bias of surface air temperature, and its simulated surface air temperature matches the observations more closely than WRF-N. Figure 9 shows analysis of net solar radiation, surface latent heat flux and sensible heat flux. It is shown that WRF-C has lower net solar radiation at surface, lower surface sensible heat flux, and higher latent heat flux than WRF-N. The aggregated effects of these energy fluxes on the surface air temperature lead to the simulated differences in surface air temperature.
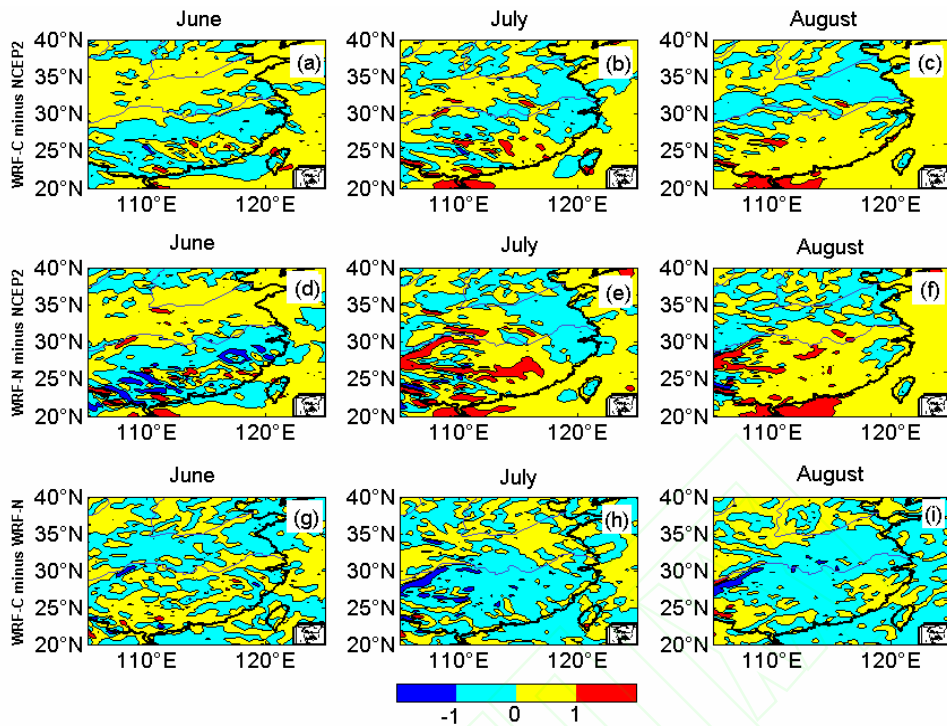
Figure 8. The difference of the Moisture Flux Convergence (MFC) of (a), (b) and (c) for WRF-C minus NCEP2, (d), (e) and (f) for WRF-N minus NCEP2, (g), (h) and (i) for WRF-C minus WRF-N, in June (left), July (middle) and August (right) 1998 (Unit: 10^{-4} kg m^{-2} s^{-2}).
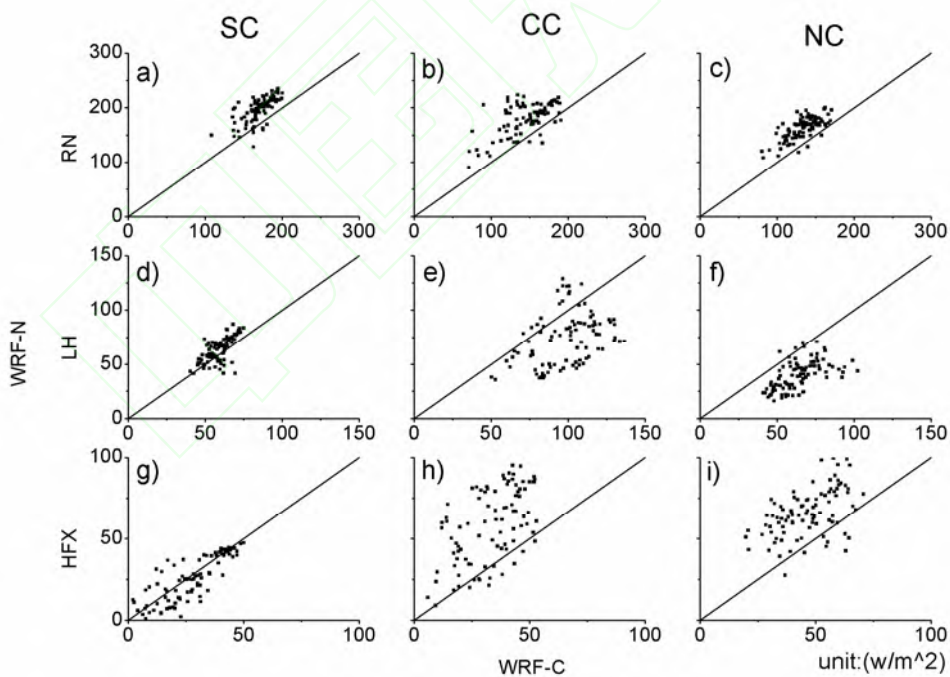

Figure 9. Net solar radiation (RN), latent heat flux (LH) and sensible heat flux (HFX) over the three subregions from the WRF-C (*x*-axises) and WRF-N (*y*-axises) simulations. Each point corresponds to each day in the summer of 1998.

4   CONCLUSIONS

In this study, the newly coupled model WRF-C, along with the existing coupled model WRF-N, were used to study the impacts of different land surface schemes on regional climate simulation. Numerical simulations were conducted by using WRF-C and WRF-N for the summer climate of a typical year (1998) over East China. We compared the simulated precipitation and surface air temperature of two land surface models that are both driven with the same atmospheric data. As a result, significant differences in simulated seasonal precipitation and surface air temperature exist in the two model simulations.

Comparisons with observational data indicate that WRF-C simulations are superior to WRF-N simulations.

As the influence of Asian monsoon decreases from south to north, the improvement of land surface schemes demonstrated most significant effect on precipitation simulations in North China, followed by the Yangtze River region and South China, respectively.

Both WRF-C and WRF-N simulated the large scale wind patterns reasonably well, with the WRF-C and WRF-N runs showing more details as compared to the NCEP reanalysis. WRF-N simulated a much stronger southwest low-level jet over the Yunnan-Guizhou Plateau than WRF-C did. Furthermore, the cyclonic air flow surrounding the Sichuan Basin in the WRF-N simulations is also stronger than in the WRF-C simulations. The cyclonic flow pattern gradually weakened from June to August. WRF-N produced excessive precipitation in June in the Sichuan Basin and Yunnan-Guizhou Plateau.

The differences between WRF-C and NCEP2 or between WRF-N and NCEP2 are consistent with the heavy rain locations, and the large positive KE difference areas correspond to the heavy rainfall areas. As WRF-C has smaller moisture convergence than WRF-N, it produces smaller amount of precipitation than WRF-N.

WRF-C had lower net solar radiation at surface, lower surface sensible heat flux, and higher latent heat flux than WRF-N. The aggregated effects of these energy fluxes on the surface air temperature lead to the simulated differences in surface air temperature. WRF-C has significantly smaller warm biases than WRF-N over most of the regions, especially over areas of Yangtze River basin and North China. WRF-C also has smaller cold biases than WRF-N over the South China area.

Here we only do the simulations on a typical year, whether similar results can be achieved for other years need to be tested. In the next study, we plan to do a longer time simulation, maybe 30 years, and to first find out the more typical years (of strong and weak monsoon) and then to assess the results of these years.

REFERENCES:

[1] LEUNG L R, MEARNS L O, GIORGI F, et al. Regional climate research: needs and opportunities [J]. Bull. Amer. Meteor. Soc., 2003, 84: 89-95.
[2] GAO Rong, DONG Wen-jie, WEI Zhi-gang. Simulation and analysis of China climate using two-way interactive atmosphere-vegetation model (RIEMS-AVIM) [J]. Adv. Atmos. Sci., 2008, 25(6): 1085-1097.
[3] ZHAO Ming. An improvement to the land surface process in RIEMS model [J]. Sci. Meteor. Sinica, 2006, 26(2): 119-126. (in Chinese)
[4] WU Qiong, YAN Xiao-dong, XIONG Zhe. The multiyear surface climatology of RIEMS over China [J]. Acta Agric. Univ. Jiangxiensis, 2009, 31(5): 950-956. (in Chinese)
[5] XIONG Zhe, WANG Shu-yu, ZENG Zhao-mei, et al. Analysis of simulated heavy rain over the Yangtze River valley during 11-30 June 1998 using RIEMS [J]. Adv. Atmos. Sci., 2003, 20(5): 815-824.
[6] XIONG Zhe. The multiyear surface climatology of RIEMS over East Asia [J]. Clim. Environ. Res., 2004, 9(2): 251-260. (in Chinese)
[7] AFIESIMAMA E, PAL J, ABIODUN B, et al. Simulation of West African monsoon using the RegCM3. Part I: Model validation and interannual variability [J]. Theor. Appl. Climatol., 2006, 86(1): 23-37.
[8] DASH S, SHEKHAR M, SINGH G. Simulation of Indian summer monsoon circulation and rainfall using RegCM3 [J]. Theor. Appl. Climatol., 2006, 86(1): 161-172.
[9] ZHANG Dong-feng, GAO Xue-jie, OUYANG Li-cheng, et al. Simulation of present climate over East Asia by a regional climate model [J]. J. Trop. Meteor., 2008, 14(1): 19-23.
[10] GAO Xue-jie, ZHANG Dong-feng, CHEN Zhong-xin, et al. Land use effects on climate in China as simulated by a regional climate model [J]. Sci. China (Ser. D: Earth Sci.), 2007, 50(4): 620-628.
[11] IM E, AHN J, REMEDIO A, et al. Sensitivity of the regional climate of East/Southeast Asia to convective parameterizations in the RegCM3 modelling system. Part 1: Focus on the Korean Peninsula [J]. Int. J. Climatol., 2008, 28(14): 1861-1877.
[12] PARK E, HONG S, KANG H. Characteristics of an East Asian summer monsoon climatology simulated by the RegCM3 [J]. Meteor. Atmos. Phys., 2008, 100(1): 139-158.
[13] ZHOU Jian-wei, WANG Yong-qing. The advance in application and research of regional climate model RegCM3 [J]. Sci. Meteor. Sinica, 2007, 27(6): 702-708. (in Chinese)
[14] CHEN Wen, ZHU De-qin, LIU Hui-zhi, et al. Land-air interaction over arid/semi-arid areas in China and its impact on the east Asian summer monsoon. Part I: Calibration of the land surface model (BATS) using multicriteria methods [J]. Adv. Atmos. Sci., 2009, 26(6): 1088-1098.
[15] HONG S, LAKSHMI V, SMALL E, et al. Effects of vegetation and soil moisture on the simulated land surface processes from the coupled WRF/Noah model [J]. J. Geophys. Res., 2009, 114(D18): D18118.
[16] QUINTANAR A, MAHMOOD R, LOUGHRIN J, et al. A coupled MM5-Noah land surface model-based assessment of sensitivity of planetary boundary layer variables to anomalous soil moisture conditions [J]. Phys. Geogr., 2008, 29(1): 54-78.
[17] CHRISTENSEN J H, RÄISÄNEN J, IVERSEN T, et al. A synthesis of regional climate change simulations—a Scandinavian perspective [J]. Geophys. Res. Lett., 2001, 28(6): 1003-1006.
[18] GIORGI F, FRANCISCO R. Evaluating uncertainties in the prediction of regional climate change [J]. Geophys. Res. Lett., 2000, 27(9): 1295-1298.
[19] PAN Z, CHRISTENSEN J, ARRITT R, et al. Evaluation of uncertainties in regional climate change simulations [J]. J. Geophys. Res., 2001, 106(D16): 17735-17751.
[20] BUKOVSKY M, KAROLY D. Precipitation simulations using WRF as a nested regional climate model [J]. J. Aappl. Meteor. Climatol., 2009, 48(10): 2152-2159.
[21] LEUNG L, QIAN Y. Atmospheric rivers induced heavy precipitation and flooding in the western US simulated by the WRF regional climate model [J]. Geophys. Res. Lett., 2009, 36(3), L03820.
[22] LEUNG L, KUO Y, TRIBBIA J. Research needs and directions of regional climate modeling using WRF and CCSM [J]. Bull. Amer. Meteor. Soc., 2006, 87(12): 1747-1751.

[23] LO J, YANG Z, PIELKE R Sr. Assessment of three dynamical climate downscaling methods using the Weather Research and Forecasting (WRF) model [J]. J. Geophys. Res., 2008, 113(D9): D09112.

[24] ZHANG Y, DULIÈRE V, MOTE P W, et al. Evaluation of WRF and HadRM Mesoscale Climate Simulations over the U.S. Pacific Northwest [J]. J. Climate, 2009, 22(20): 5511-5526.

[25] OLESON K, DAI Y, BONAN G, et al. Technical description of the community land model (CLM), NCAR Tech [R]. Note NCAR/TN-461+STR. 2004: 186pp.

[26] DICKINSON R, HENDERSON-SELLERS A, KENNEDY P, et al. Biosphere¨Catmosphere transfer scheme (BATS) version 1e as coupled to the NCAR Community Climate Model [R]. NCAR Tech., Note, NCAR/TN387+ STR, 1993.

[27] BONAN G. Land surface model (LSM version 1.0) for ecological, hydrological, and atmospheric studies: Technical description and users guide [R]. National Center for Atmospheric Research Tech. Note, NCAR/TN-417+STR, 1996: 88-102.

[28] DAI Yong-jiu, ZENG Qing-cun. A land surface model (IAP94) for climate studies Part I: Formulation and validation in off-line experiments [J]. Adv. Atmos. Sci., 1997, 14(4): 433-460.

[29] MITCHELL K, COLLAHNRATOM. The Community NOAH Land Surface Model User's Guide [M/OL]. ftp://ftp.emc.ncep.noaa.gov/mmb/qcp/ldas/noahlsm/ver 2.5.2/, 2002.

[30] JIN J, MILLER N L. Impacts of land use change on the local climate over the California Central Valley using WRF-CLM3 [C]// AGU Fall 2005 Conference, San Francisco, CA., 2005.

[31] JIN J, MILLER N L, SCHLEGEL N J. Understanding the role of land surface processes in WRF-CLM3 [C]// WRF Workshop 2007.

[32] JIN J, WEN L, SUBIN Z M, et al. Calibration and Validation of WRF 3.0-CLM3.5 in Snowpack Simulations [C]// American Geophysical Union, Fall Meeting 2009, abstract #H42C-07.

[33] HUFFMAN G, ADLER R, ARKIN P, et al. The global precipitation climatology project (GPCP) combined precipitation dataset [J]. Bull. Amer. Meteor. Soc., 1997, 78(1): 5-20.

[34] HUANG Gang. An index measuring the interannual variation of the East Asian summer monsoon: The EAP index [J] Adv. Atmos Sci., 2004, 21(1): 41-52.

[35] WU Shang-sen, LIANG Jian-yin. An index of South China Sea summer monsoon intensity and its variation characters [J]. J. Trop. Meteor., 2001, 17(4): 337-344. (in Chinese)

[36] ZENG X, SHAIKH M, DAI Y, et al. Coupling of the Common Land Model to the NCAR Community Climate Model [J]. J. Climate, 2002, 15: 1832-1854.

[37] ZHANG Qing. Some Characteristics of Weather/Climate in China in 1998 [M]. Meteor. Mon., 1999, (4): 27-30. (in Chinese)

[38] BANACOS P C, SCHULTZ D M. The use of moisture flux convergence in forecasting convective initiation: Historical and operational perspectives [J]. Wea. Forecast., 2005, 20: 351-366.

[39] CASTRO C L, PIELKE SR R A, LEONCINI G. Dynamical downscaling: Assessment of value retained and added using the Regional Atmospheric Modeling System (RAMS) [J]. J. Geophys. Res., 2005, 110, D05108, doi:10.1029/2004JD004721.